Inorganic Chemistry

pubs.acs.org/IC Article

Electronic Structure and Magnetic Properties of a Low-Spin Cr^{II} Complex: *trans*-$[CrCl_2(dmpe)_2]$ (dmpe = 1,2-Bis(dimethylphosphino)ethane)

Eva M. Zolnhofer, Adedamola A. Opalade, Timothy A. Jackson,* Frank W. Heinemann, Karsten Meyer, J. Krzystek, Andrew Ozarowski, and Joshua Telser*

Cite This: *Inorg. Chem.* 2021, 60, 17865−17877 Read Online

ABSTRACT: Octahedral coordination complexes of the general formula *trans*-$[MX_2(R_2ECH_2CH_2ER_2)_2]$ (M^{II} = Ti, V, Cr, Mn; E = N, P; R = alkyl, aryl) are a cornerstone of both coordination and organometallic chemistry, and many of these complexes are known to have unique electronic structures that have been incompletely examined. The *trans*-$[CrCl_2(dmpe)_2]$ complex (dmpe = $Me_2PCH_2CH_2PMe_2$), originally reported by Girolami and co-workers in 1985, is a rare example of a six-coordinate d^4 system with an $S = 1$ (spin triplet) ground state, as opposed to the high-spin ($S = 2$, spin quintet) state. The ground-state properties of $S = 1$ systems are challenging to study using conventional spectroscopic methods, and consequently, the electronic structure of *trans*-$[CrCl_2(dmpe)_2]$ has remained largely unexplored. In this present work, we have employed high-frequency and -field electron paramagnetic resonance (HFEPR) spectroscopy to characterize the ground-state electronic structure of *trans*-$[CrCl_2(dmpe)_2]$. This analysis yielded a complete set of spin Hamiltonian parameters for this $S = 1$ complex: $D = +7.39(1)$ cm^{-1}, $E = +0.093(1)$ ($E/D = 0.012$), and $\mathbf{g} = [1.999(5), 2.00(1), 2.00(1)]$. To develop a detailed electronic structure description for *trans*-$[CrCl_2(dmpe)_2]$, we employed both classical ligand-field theory and quantum chemical theory (QCT) calculations, which considered all quintet, triplet, and singlet ligand-field states. While the high density of states suggests an unexpectedly complex electronic structure for this "simple" coordination complex, both the ligand-field and QCT methods were able to reproduce the experimental spin Hamiltonian parameters quite nicely. The QCT computations were also used as a basis for assigning the electronic absorption spectrum of *trans*-$[CrCl_2(dmpe)_2]$ in toluene.

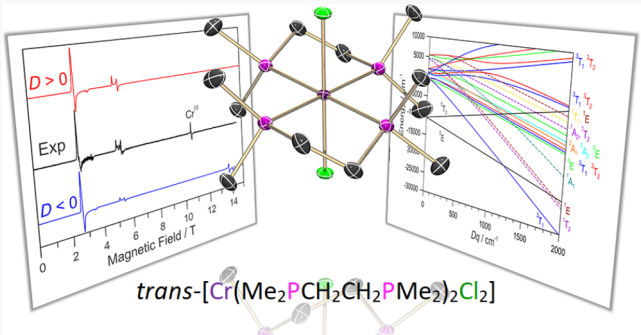

■ INTRODUCTION

Chelating ligands, $R_2E(CH_2)_nER_2$ (E = group 15 donor; n = 1−3; R = H, alkyl, aryl), have played an important and historical role in coordination and organometallic chemistry. The size of the chelate ring is controlled by n, wherein $n = 2$ forms the stable five-membered metal-chelate ring and is the most commonly employed. The σ-donor and π-acceptor properties of E are controlled by period, with E = N being the classical coordination chemistry ligand (e.g., R = H gives ethylenediamine, en) with no π-bonding and E = P being the classical organometallic ligand series (e.g., R = Me giving dmpe, 1,2-bis(dimethylphosphino)-ethane, and R = Ph giving dppe, 1,2-bis(diphenylphosphino)-ethane) with π-acceptor properties. In a landmark paper, Girolami, Wilkinson, and co-workers reported a series of first-row divalent transition-metal dmpe complexes of general formula *trans*-$[MX_2(Me_2PCH_2CH_2PMe_2)_2]$, where M^{II} = Ti, V, Cr, Mn and X = Me, Cl, Br.[1−3] Subsequent studies by Girolami and co-workers explored the chemistry of *trans*-$[TiX_2(Me_2PCH_2CH_2PMe_2)_2]$ (X = Me,[4] OPh,[5] η^2-BH_4[6]) and of *trans*-$[VX_2(Me_2PCH_2CH_2PMe_2)_2]$ (X = η^1-BH_4,[6] Me[7]) Previously reported complexes of Ti^{II} with the same tetragonal geometry,[8,9] but with nitrogen donor ligands, have been recently explored by us. These are *trans*-$[TiCl_2(py)_4]$ (py = pyridine)[10] and *trans*-$[TiCl_2(tmeda)_2]$ (tmeda = *N,N,N′,N′*-tetramethylethane-1,2-diamine = $Me_2NCH_2CH_2NMe_2$).[11,12] A theme that is pervasive in these studies, and of importance for practical applications,[13] is the variation in spin ground state among related complexes. For example, the spin ground state of *trans*-$[TiX_2(Me_2PCH_2CH_2PMe_2)_2]$ is a function of the axial ligand, wherein X = Cl,[1] η^2-BH_4[6] have the triplet ground state expected for d^2, but for X = Me,[4] OPh[5] the ground state is a singlet (diamagnetic).

Received: August 12, 2021
Published: November 1, 2021

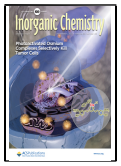

https://doi.org/10.1021/acs.inorgchem.1c02471
Inorg. Chem. 2021, 60, 17865−17877

Even within triplet complexes, there is variation in that the ground state in *trans*-[$TiCl_2(py)_4$] is doubly degenerate (^3E_g in D_{4h} ideal symmetry),[10] while that of *trans*-[$TiCl_2(tmeda)_2$] is singly degenerate (^3A_g in D_{2h} ideal symmetry).[11]

Our current interest is not to discuss further the differences among these *trans*-[$Ti^{II}X_2(L)_2$] complexes but to use these as an inspiration for moving to the next even-electron-count 3d dication, namely Cr^{II}, as found in *trans*-[$CrCl_2(Me_2PCH_2CH_2PMe_2)_2$], hereafter *trans*-[$CrCl_2(dmpe)_2$]. This complex is of interest not only as another member of the *trans*-[$MX_2(L)_2$] series but also for its low spin (in an octahedral sense;[14−16] in D_{4h} symmetry, $S = 0$ is viable if the e_g orbitals (d_{xz}, d_{yz}) are sufficiently lower in energy than the b_{2g} orbital (d_{xy}))[15,16] ground state, in contrast to typical octahedral Cr^{II}, such as that found in $[Cr(H_2O)_6]^{2+}$.[17−19] We have previously studied an "octahedrally low-spin" d^4 system, in that case with trigonal distortion, namely Mn^{III} supported by bis(scorpionate) ligands, of both the "traditional" hydro-(trispyrazolyl)borate and "carbene" phenyl(trisimidazolyl)-borate type.[20] Again, these $S = 1$ d^4 systems are in the minority, as such Mn^{III} complexes typically exhibit an $S = 2$ ground state. The complex *trans*-[$CrCl_2(dmpe)_2$] thus provides a tetragonal example of this electronic configuration and is in a 2+ oxidation state. This lower oxidation state, combined with relatively weak axial ligands (chloride, as opposed to e.g., methyl, as in the Ti^{II} example above), which are cylindrical π-donors, as opposed to more π-anisotropic ligands (e.g., phenoxide) make the triplet ground state intriguing. To achieve our goal of understanding the electronic structure of *trans*-[$CrCl_2(Me_2PCH_2CH_2PMe_2)_2$], we can apply experimental (high-frequency and -field electron paramagnetic resonance (HFEPR) spectroscopy) and computational (*ab initio* quantum chemical theory (QCT)) methods that were unavailable when these types of *trans*-[$MX_2(Me_2ECH_2CH_2EMe_2)_2$] complexes were originally reported near the end of the last century. The key contribution of HFEPR in such systems is the accurate and precise determination of zero-field splitting (ZFS) parameters (for systems with $S > 1/2$),[21,22] which are very sensitive metrics of electronic structure, as well as being a crucial phenomenon in the function of single-molecule magnets (SMMs).[23] Moreover, in the previously studied $S = 1$ Mn^{III} complexes, the electronic absorption spectra were relatively uninformative,[20] which is not the case for *trans*-[$CrCl_2(Me_2PCH_2CH_2PMe_2)_2$], but those spectra had not been analyzed.[1] This study specifically on *trans*-[$CrCl_2(dmpe)_2$] also provides generally applicable information on the bonding effects of the widely used dmpe ligand.

■ EXPERIMENTAL SECTION

General Considerations. The manipulation of air-sensitive compounds was performed using standard Schlenk-line techniques or an MBraun inert-gas glovebox containing an atmosphere of purified dinitrogen or argon where specified. Solvents were purified using a two-column solid-state purification system (Glasscontour System, Joerg Meyer, Irvine, CA), transferred to the glovebox without exposure to air, and stored over activated molecular sieves and/or sodium metal. NMR solvents were dried over Na/K alloy or molecular sieves and distilled under reduced pressure and/or filtered through a column of neutral activated aluminum oxide. Elemental analysis results were obtained from the Analytical Laboratories at FAU-Erlangen-Nürnberg, using Euro EA 3000 (Euro Vector) and EA 1108 (Carlo-Elba) elemental analyzers. Electronic absorption spectra of *trans*-[$CrCl_2(dmpe)_2$] were recorded on a Shimadzu UV-3600 UV−vis−NIR spectrophotometer in toluene solution at room temperature.

Synthesis of *trans*-[$CrCl_2(dmpe)_2$]. The general procedure of Girolami et al. was used.[1] Under a nitrogen atmosphere, $CrCl_2$ (40.6 mg, 0.33 mmol, 1 equiv) was suspended in toluene (1.8 mL). Immediately after addition of dmpe (0.09 mg, 0.1 mL, 0.66 mmol, 2 equiv), a color change from light green to intense apple green was observed. The solution was stirred for 2 h, concentrated to a volume of 1.5 mL, and cooled to −35 °C overnight, affording green crystals that were collected by filtration, washed with a few drops of cold (−35 °C) toluene, and dried. A second crop was obtained by further concentration of the filtrate, cooling, filtration, washing, and drying as with the first crop (65 mg, 47%). Anal. Calcd for $C_{12}H_{32}Cl_2CrP_4$ (MW = 423.18 g/mol): C, 34.06; H, 7.62. Found: C, 34.28; H, 7.53.

X-ray Crystallography. Details of the X-ray crystallography of *trans*-[$CrCl_2(dmpe)_2$] collected at 100 K, are given in Section S1 in the Supporting Information. Figure S2 shows crystal packing diagrams for this complex, demonstrating that there are no intermolecular interactions.

Magnetometry. Magnetometry data of crystalline, finely powdered *trans*-[$CrCl_2(dmpe)_2$] restrained within a polycarbonate gel capsule were recorded with a Quantum Design MPMS-XL SQUID magnetometer (FAU-Erlangen-Nürnberg). DC susceptibility data for two separate samples (15.0 and 6.5 mg, respectively) of *trans*-[$CrCl_2(dmpe)_2$] were collected in the temperature range of 2−300 K under a DC field of 1 T. Values of the magnetic susceptibility were corrected for the core diamagnetism of the sample estimated using tabulated Pascal's constants.[24] The program DSUSFITP (J. Telser) was used for fitting magnetic susceptibility data using a standard $S = 1$ spin Hamiltonian.

High-Frequency and -Field EPR Spectroscopy (HFEPR). HFEPR data were acquired using the EMR Facility of the NHMFL. Details are provided in Section S2 in the the Supporting Information.

Computational Methods. Ligand field theory (LFT) calculations employed locally written (J. Telser) programs and Ligfield (J. Bendix).[25] All quantum chemical theory (QCT) calculations were performed using ORCA 4.2.1.[26,27] Details are provided in Sections S3 (LFT) and S4 (QCT) in the Supporting Information, respectively.

■ RESULTS AND ANALYSIS

Single Crystal X-ray Diffraction (XRD). The crystal structure of *trans*-[$CrCl_2(dmpe)_2$] was previously reported by Girolami et al. (CSD code: DAJDUN).[1] This had been determined at room temperature; therefore, a low-temperature (100 K) structure was determined here for overall confirmation as well as better comparison with low-temperature, solid-state HFEPR spectroscopy and computational studies. The structure is shown in Figure 1; Figures S1 and S2 in the Supporting Information respectively show the structures of both crystallographically independent molecules and the crystal packing.

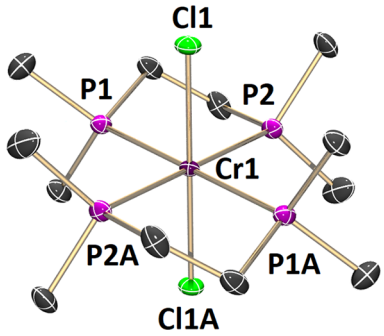

Figure 1. Molecular structure of *trans*-[$CrCl_2(dmpe)_2$]. Thermal ellipsoids are drawn at 50% probability, and H atoms are omitted for clarity. Only molecule 1 of the two crystallographically independent molecules is shown. See Figures S1 and S2 in the Supporting Information for further crystal structure representations.

https://doi.org/10.1021/acs.inorgchem.1c02471
Inorg. Chem. 2021, 60, 17865−17877

Crystallographic information is given in Table S1. The differences between the previous room-temperature and current 100 K structures are minimal. Table S2 summarizes the relevant metrics for a wide series of complexes of the general formula *trans*-$[CrX_2(R_2PCH_2CH_2PR_2)_2]^{0,2+}$, where R = Me, Et, Ph and X = a wide range of monoanionic ligands. The structure reported by Ricci et al.[28] of *trans*-$[CrCl_2(depe)_2]$ (depe = 1,2-bis(diethylphosphino)ethane, $Et_2PCH_2CH_2PEt_2$) is almost the same as that of the dmpe complex, with only a slight decrease in P−Cr−P chelate angle, 81.77° versus 82.84° (average of the present and previous dmpe structure values), which may be due to the larger steric requirements of the depe ligand.

In contrast to *trans*-$[TiCl_2(tmeda)_2]$,[11] the M−Cl and M−E (E = N for tmeda; E = P for dmpe) bond lengths are very close in the Cr structure, a consequence of all the donor atoms being from period 3 in the present study. The relevant, averaged metrics (in Å) are as follows: *trans*-$[TiCl_2(tmeda)_2]$, d(Ti−Cl) = 2.51, d(Ti−N) = 2.38; *trans*-$[CrCl_2(dmpe)_2]$, d(Cr−Cl) = 2.35, d(Cr−P) = 2.37. The key crystallographic feature for the present purposes of electronic structure analysis is the same as that in the previously studied complex *trans*-$[TiCl_2(tmeda)_2]$: namely, that the Cl−M−Cl angle is 180° and that the Cl−Cr−E (E = P here) angles average 90° (with a range of ∼±2°; see Table S2). Thus, a tetragonally distorted octahedral coordination describes this Cr^{II} complex well, as was the case for Ti^{II}.[11] The chelate effect of $Me_2ECH_2CH_2EMe_2$ (here, E = P) leads to an orthorhombic distortion (∠P−M−P < 90°), so that the idealized molecular point group symmetry is D_{2h}; however, D_{4h} is generally sufficient, as will be discussed below.

Magnetometry. As noted above, *trans*-$[CrCl_2(dmpe)_2]$ is approximately octahedral, so that for Cr^{II} ($3d^4$), a high-spin (spin quintet) ground state might be expected (S = 2; $t_{2g}^3e_g^1$ in strong-field notation). For comparison, the congener *trans*-$[VCl_2(dmpe)_2]$, which contains V^{II} ($3d^3$), has an S = 3/2 ground state as expected ($t_{2g}^3e_g^0$ in strong-field notation) and its room-temperature susceptibility in toluene solution gave μ_{eff} = 3.7(1) (unitless[29]);[1] the S = 3/2 spin-only value with g = 1.91—a reasonable value for a less than half-filled system. Likewise, the Ti^{II} congener *trans*-$[TiCl_2(dmpe)_2]$ has an S = 1 ground state ($t_{2g}^2e_g^0$ in strong-field notation) as expected for octahedral d^2 and its room-temperature solution susceptibility gave μ_{eff} = 2.9(1),[1] the spin-only value with g = 2.05—somewhat high but not disturbingly so. In contrast, *trans*-$[CrCl_2(dmpe)_2]$ has an S = 1 spin ground state ($t_{2g}^4e_g^0$ in strong-field notation), and its room-temperature susceptibility in toluene solution is μ_{eff} = 2.8(1), which corresponds to the S = 1 spin-only value with g = 1.98. We have measured the variable-temperature (2−300 K) DC susceptibility of powdered *trans*-$[CrCl_2(dmpe)_2]$ and confirmed the spin triplet behavior. Consistent with the room-temperature solution study, $\chi_M T$ is essentially constant over the range $30 \leq T \leq 300$ K and can be fitted with g_{iso} = 2.008, slightly higher than the solution value, as explained below. At T < 30 K, $\chi_M T$ decreases due to ZFS, which can be fitted using axial magnetic anisotropy (i.e., E = 0), as shown in Figure 2. In this case, the fit quality is highly sensitive to the sign of D. Fits using a positive D value were superior to those with negative D, in terms of both the error and the g value being unreasonably large for D < 0. Thus, magnetic data alone yield S = 1 with D = +7.3 cm^{-1} and g_{iso} = 2.01 for *trans*-$[CrCl_2(dmpe)_2]$. As will be shown below, HFEPR provides superior spin Hamiltonian parameters for this complex, which can be applied to the magnetic data. The low-temperature data are well fitted by the HFEPR parameters, but $\chi_M T$ for the high-temperature data ($30 \leq T \leq 300$ K) are slightly

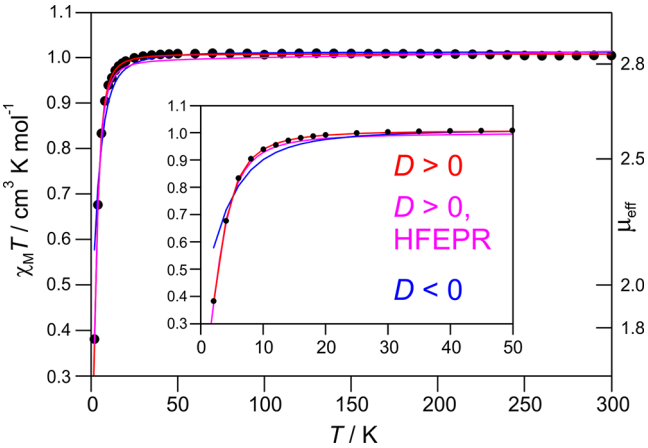

Figure 2. Variable-temperature DC magnetic susceptibility of powdered *trans*-$[CrCl_2(dmpe)_2]$. The inset shows an expansion of the lower temperature region. Experimental points are shown as circles and fits using the S = 1 spin Hamiltonian as solid lines. Red trace: fit with D = +7.305 cm^{-1}, g_{iso} = 2.0086. Blue trace: fit with D = −12.086 cm^{-1}, g_{iso} = 2.0130. Magenta trace: fit with D = +7.360 cm^{-1}, E = +0.005 cm^{-1}, $g_\perp$ = 1.998, $g_\parallel$ = 1.989, TIP = 63.6 × 10^{-6} cm^3 mol^{-1}. The parameters used to generate the magenta trace are fixed from HFEPR (see below) with TIP determined by fitting.

too low, by ∼1.3%. This can be addressed by inclusion of a small temperature-independent paramagnetism (TIP) term, which is justified as it can account for excited states, such as those with S = 2.[30] There is then an improved match between the magnetic susceptibility data over the full temperature range and the HFEPR results for the S = 1 Cr^{II} complex.

HFEPR Spectroscopy. HFEPR was initially performed on powdered samples of *trans*-$[CrCl_2(dmpe)_2]$. Due to the complex's air sensitivity, these studies were conducted on material that was left intact as microcrystals. As a result, an ideal powder pattern (i.e., random distribution) was not obtained; rather, there were narrow signals from individual microcrystallites, as we have seen previously.[20] Nevertheless, it was clear that *trans*-$[CrCl_2(dmpe)_2]$ gave a strong HFEPR response and that the signals arose from a spin triplet as shown in Figure S3. At higher temperature (30 K), the individual crystallite line widths increased so that the spectral appearance was more like a powder pattern (Figure S4) and spin Hamiltonian parameters could be extracted by simulation of the 203 GHz spectrum shown therein. These parameters (chiefly, $|D|$ = 7.38 cm^{-1}) match the HFEPR spectrum at the highest available VDI diode source frequency (406 GHz, Figure S5), but because of the relatively high temperature it was still not possible to determine the sign of D. A 2D data set of resonant field position versus frequency (energy) shown in Figure S6 allows for a global fit for the spin Hamiltonian parameters for solid *trans*-$[CrCl_2(dmpe)_2]$: $|D|$ = 7.36(2) cm^{-1}, $|E|$ = 0.005(10), $g_\perp$ = 1.998(5), and $g_\parallel$ = 1.989(7). These values were used to successfully fit the DC susceptibility (Figure 2), with D > 0, as required by the magnetometry fits and determined from frozen solution (*vide supra*).

To determine the spin Hamiltonian parameters of isolated *trans*-$[CrCl_2(dmpe)_2]$, and to assign the sign of D, HFEPR spectra were subsequently recorded of the complex in a frozen toluene/dichloromethane (1/2 v/v) solution. A representative spectrum, recorded at 295 GHz and 4.5 K, is shown in Figure 3. It is clear from the relative intensities of the signals at ∼5 T

https://doi.org/10.1021/acs.inorgchem.1c02471
Inorg. Chem. 2021, 60, 17865−17877

versus those at ∼14 T that D is positive. Consequently, and by convention, the sign of E is given as positive.

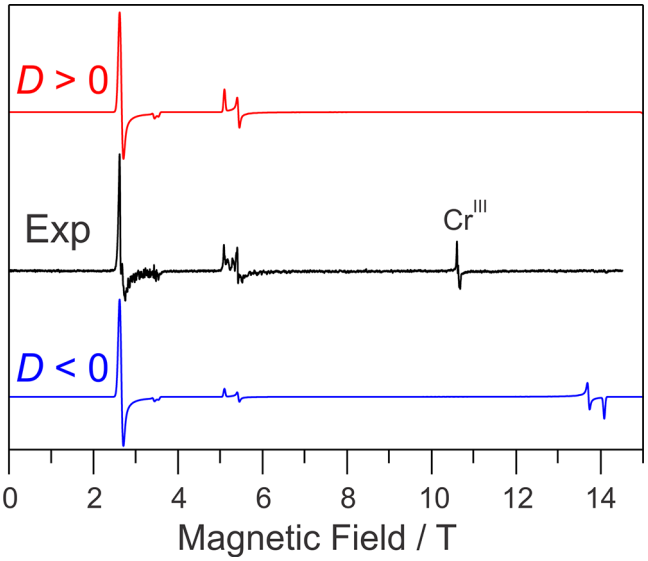

Figure 3. HFEPR spectrum of a frozen solution (toluene/dichloromethane) of *trans*-$[CrCl_2(dmpe)_2]$ at 295 GHz and 4.5 K (black trace). The $S = 1$ simulation parameters are $|D| = 7.38$ cm^{-1}, $|E| = 0.103$ cm^{-1}, $g_{iso} = 2.00$; red trace with $D > 0$ and blue trace with $D < 0$. The experimental and simulated spectra are normalized to the height of the B_{min} signal and leave no doubt that D is positive. A signal from a Kramers (half-integer spin) impurity (presumably Cr^{III}) is observed at ∼10.6 T ($g \approx 1.985$). The integrated intensity of this narrow and isotropic signal is minimal in comparison to that of the compound of interest, which covers a ∼12 T field range.

An additional, higher-frequency (403 GHz) frozen solution HFEPR spectrum is shown in Figure S7, and it further confirms the positive sign of D. As with the solid-state data, global fitting of a 2D field-frequency plot, shown in Figure 4, yields a final set of spin Hamiltonian parameters for a frozen solution of *trans*-$[CrCl_2(dmpe)_2]$: $D = +7.39(1)$ cm^{-1}, $E = +0.093(1)$, $g_x = 1.999(5)$, $g_y = 2.00(1)$, $g_z = 2.00(1)$, where the positive sign is derived from individual spectra (e.g., Figure 3 and Figure S7).

A final confirmation of the positive sign of D comes from the temperature dependence of the HFEPR spectra, as shown in Figure S8. The allowed ($\Delta m_S = \pm 1$) excited state $|S, m_S\rangle = |1, 0\rangle \leftrightarrow |1, +1\rangle$ originated transition at ∼14 T (see also Figure 3) grows in intensity as the temperature is increased, while the ground state $|S, m_S\rangle = |1, -1\rangle \leftrightarrow |1, 0\rangle$ originated transition at ∼5 T (see also Figure 3) decreases in intensity. If D were negative, then the intensity behavior would be reversed. It is also useful to point out that Figure S8 shows no detectable change in the spin Hamiltonian parameters between 5 and ∼80 K, so that the structures determined for *trans*-$[CrCl_2(dmpe)_2]$ by XRD at 100 K (this work) and ∼300 K (Girolami et al.[1]) are the same as those at the liquid He temperatures used for the bulk of the HFEPR measurements. The correspondence of the VT magnetic susceptibility data with HFEPR also supports this assumption.

Electronic Absorption Spectroscopy. The complex *trans*-$[CrCl_2(dmpe)_2]$ is yellow-green[1] to green, a color often associated with Cr^{III} but is purely coincidental in this low-spin Cr^{II} case. The electronic absorption spectrum of *trans*-$[CrCl_2(dmpe)_2]$ at room temperature in toluene solution is shown in Figure 5. There is a strong charge transfer (CT) band

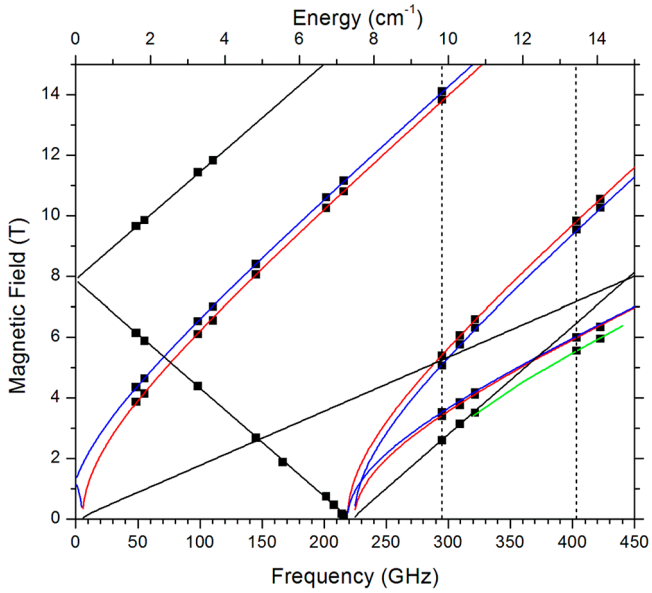

Figure 4. Field vs frequency (energy) map of turning points (shown as squares) in a frozen solution of *trans*-$[CrCl_2(dmpe)_2]$ at 4.5 K. The best-fit $S = 1$ spin Hamiltonian parameters are $|D| = 7.39(1)$ cm^{-1}, $E = 0.093(1)$, $g_x = 1.999(5)$, $g_y = 2.00(1)$, and $g_z = 2.00(1)$. Black lines correspond to turning points with $B_0 \| z$, red lines to $B_0 \| x$, and blue lines to $B_0 \| y$. The green line corresponds to an off-axis *extremum*, which is also simulated. The dashed vertical lines represent the frequencies (295 and 403 GHz) at which the spectra shown in Figure 3 and Figure S7, respectively, were recorded.

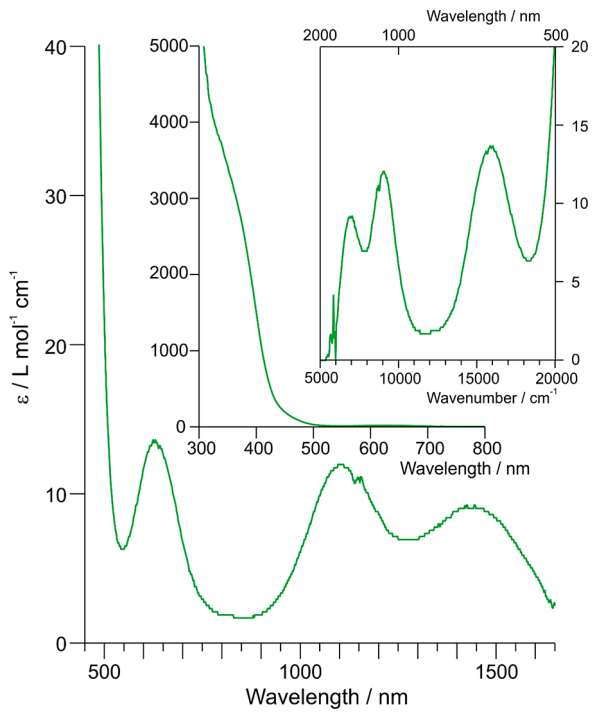

Figure 5. Electronic absorption spectrum of *trans*-$[CrCl_2(dmpe)_2]$ in toluene solution at room temperature. The main figure shows the visible and NIR regions, the first inset shows the UV and visible regions, both on wavelength scales, and the second, boxed, inset shows the visible and NIR regions on a wavenumber scale. The ordinate is in molar absorption coefficient in all cases.

(shoulder) in the near-UV region (∼350 nm, $\varepsilon \approx 3000$ mol^{-1} L cm^{-1}; Figure 5, inset) and three bands assignable to d−d

https://doi.org/10.1021/acs.inorgchem.1c02471
Inorg. Chem. 2021, 60, 17865−17877

transitions, one in the visible region (629 nm (15900 cm^{-1}), ε = 13 mol^{-1} L cm^{-1}) and two in the NIR region (1104 nm (9060 cm^{-1}), ε = 12 mol^{-1} L cm^{-1}; 1432 nm (6980 cm^{-1}), ε = 9 mol^{-1} L cm^{-1}). The assignment of these bands will be discussed in the following section.

Ligand Field Theory: Electronic Transitions and ZFS Parameters. The spin-allowed electronic transitions in an octahedral high-spin d^4 system are straightforward, as there is only one free-ion quintet term, ^5D. In contrast, there is a large number of free-ion triplet terms: ^3H, ^3G, ^3F_a, ^3F_b, ^3D, ^3P_a, and ^3P_b. In addition, there are eight free-ion singlet terms, which are typically ignored in high-spin d^4 but can be relevant in the octahedral low-spin case: ^1I, ^1G_a, ^1G_b, ^1F, ^1D_a, ^1D_b, ^1S_a, and ^1S_b. Given that an octahedral, here with tetragonal distortion, low-spin d^4 configuration is relatively uncommon, we begin by generating a Tanabe–Sugano type of diagram that probes the free-ion term origin of the lower energy states in octahedral symmetry. The free-ion Racah interelectronic repulsion parameters of Cr^{II} are B = 796 cm^{-1} and C = 3298 cm^{-1} (C/B = 4.14).[31] These values must be substantially reduced (the nephelauxetic effect) for the ground state to become a spin triplet. For illustrative purposes, we use B = 500 cm^{-1} and C = 2000 cm^{-1} (C/B = 4.0), i.e., just over 60% of the free-ion values, which is appropriate in the "Goldilocks" model, in that a larger nephelauxetic effect would favor low spin even with weak-field ligands (e.g., H_2O), while a lesser effect would not give a low spin unless the ligands were extremely strong field (e.g., CN^-). The resulting term energies in O_h symmetry are shown in Figure 6, with a complete depiction given in Figure S10 in the Supporting Information. For completeness, a diagram such as in Figure 6 was generated using B = 600 cm^{-1} and C = 2500 cm^{-1} (C/B = 4.17), i.e., ~75% of the free-ion values, which gives qualitatively the same results as shown here (Figure S11 in the Supporting Information). It can be seen that the high-spin term $^5E_g(^5D)$ ($t_2^3e^1$ in strong-field notation) persists as the ground state until $10Dq$ (Δ_o) ≈ 12000 cm^{-1}, which corresponds to a relatively modest octahedral field. Thereafter, the ground state is $^3T_{1g}$ ($t_2^4e^0$).[32] Indeed, at $10Dq$ ≈ 18000–19000 cm^{-1}, also not an excessively strong field, two singlet states ($^1T_{2g}$ and ^1E_g, both $t_2^4e^0$, of course) become lower in energy than $^5E_g(^5D)$. These both originate in ^1I but are very mixed, mainly with $^1G_{a,b}$ and $^1D_{a,b}$, respectively, at Dq = 2000 cm^{-1}. We have thus identified the ground state in *trans*-[$CrCl_2(dmpe)_2$], albeit in an idealized O_h symmetry. The next item is to identify triplet excited states that might be those involved in the observed bands (Figure 5). It is clear from Figure 6 that there are no triplet excited states that would yield spin-allowed transitions in the NIR region (i.e., none within 10000 cm^{-1}). These bands must either be spin-forbidden or involve the tetragonal splitting present within the actual geometry of the complex. The absorption band in the visible region (15900 cm^{-1}), however, could be related to a spin-allowed transition. Figure 6 shows six possible triplet excited state candidates, in pairs of three, in ascending energy order, $^3E_g(^3H,^3G)$, $^3T_{1g}(^3H,^3G,^3P)$, and $^3T_{2g}(^3H,^3F)$, all closely separated, and then $^3A_{1g}(^3G)$, $^3A_{2g}(^3F_b)$, and $^3E_g(^3G,^3D)$ ($t_2^3e^1$), also closely separated.[33] All other triplet excited states are much higher in energy. Note that these six triplet excited states are all $t_2^3e^1$ in strong field and, thus, track linearly with an octahedral field (for $Dq \gtrsim 400$ cm^{-1}), as does the ground state (albeit with a different, greater slope). Thus, their relative ordering is constant, regardless of the value of Dq. Figure 6 also shows using arrows, corresponding to the energy of the band at 15900 cm^{-1}, assignments that bracket the range 1400 $cm^{-1} \leq Dq \leq$ 1800 cm^{-1}, which give viable spin-allowed transitions. For example, using Dq = 1509 cm^{-1}, it is possible to match exactly this band to $^3T_{1g}(^3H) \rightarrow {}^3A_{2g}(^3F)$, which is roughly in the middle of this group of triplet excited states. Note that these excited states span all representations, A_{1g}, A_{2g}, E_g, T_{1g}, and T_{2g}, so any symmetry/polarization could in principle be possible. All $g \rightarrow g$ transitions in O_h are technically dipole forbidden, but the use of point group O shows that $T_1 \rightarrow A_1$, E, T_1, and T_2 are dipole allowed, with only $T_1 \rightarrow A_2$ being forbidden.

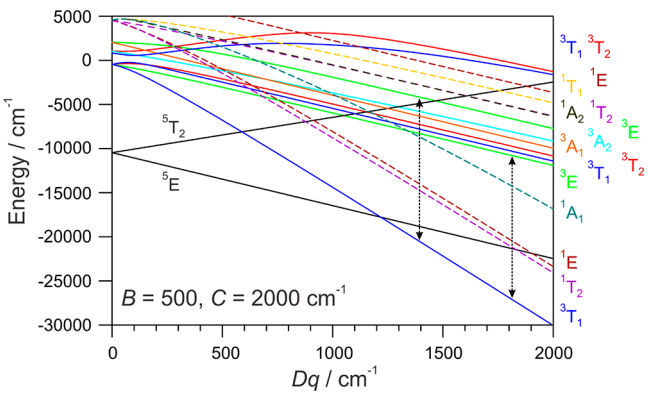

Figure 6. Energy level diagram for d^4 in O_h symmetry (g subscripts are omitted for clarity) calculated using Racah B = 500 cm^{-1} and C = 2000 cm^{-1} with cubic crystal field splitting, Dq, varying on the abscissa. The two quintet states originating from ^5D are shown in black, triplets are shown as colored solid lines, and singlets are shown as colored dashed lines. Some high-energy states that would appear in part on the diagram are omitted. See Figure S10 for a more complete diagram and Figures S9 and S11 for calculations using B = 400 cm^{-1}, C = 1600 cm^{-1} and B = 600 cm^{-1}, C = 2500 cm^{-1}, respectively. Triplet and singlet free-ion terms are not indicated, but ^3H is the lowest energy among these on the ordinate, while ^3P, ^3F, and ^3G on the ordinate are in the range 750–2000 cm^{-1} and ^1I, ^1G, and ^3D are clustered near 5000 cm^{-1}. The two arrows represent possible assignments of the observed band in the visible region (15900 cm^{-1}), corresponding to the lower and upper ranges of Dq.

The band at 15900 cm^{-1} can be fitted in multiple ways with O_h symmetry, as indicated by Figure 6 (and Figures S9–S11). Assigning this band to $^3T_{1g} \rightarrow {}^3T_{2g}$ gives B = 430 cm^{-1} (54% of the free-ion value;[31] $C/B \equiv 4$ for this simplistic fit) and ε_σ = 5530 cm^{-1}. Assignment to $^3T_{1g} \rightarrow {}^3A_{1g}$ gives B = 570 cm^{-1} (72% of the free-ion value[31]) and ε_σ = 5200 cm^{-1}.[34] Thus, B = 500 ± 70 cm^{-1} and ε_σ = 5400 ± 400 cm^{-1} cover the range of possibilities. The next step is to attempt to assign the NIR transitions, which must necessarily be spin forbidden in O_h (see Figure 6 and Figures S9–S11). Retaining the assignment $^3T_{1g} \rightarrow {}^3A_{1g}$ for the band in the visible region allows fitting the lower energy band in the NIR region to $^3T_{1g} \rightarrow {}^1T_{2g}$ (see Figure 6) with B = 609 cm^{-1} (76% of the free-ion value[31]) and ε_σ = 5179 cm^{-1} (essentially unchanged). At the other end of the range, $^3T_{1g} \rightarrow {}^3T_{2g}$ is successful only if the lower energy NIR band is assigned to $^3T_{1g} \rightarrow {}^5E_g$, which can be achieved with B = 384 cm^{-1} (48% of the free-ion value[31]), thus verging on the low side, and ε_σ = 5513 cm^{-1} (essentially unchanged) so that $10Dq$ ≈ 16000 cm^{-1} covers these possibilities.

Given this viable model for the overall electronic structure of *trans*-[$CrCl_2(dmpe)_2$] in idealized O_h symmetry, we shift to a more realistic geometrical description via the angular overlap model (AOM), as shown in Figure S12. We employ idealized D_{4h} symmetry, meaning that all angles (∠Cl–Cr–P and ∠P_i–

https://doi.org/10.1021/acs.inorgchem.1c02471
Inorg. Chem. 2021, 60, 17865–17877

Cr−P_j) are set equal to 90°. We also assume that the two chlorido ligands are equivalent, which is reasonable given their crystallographically imposed symmetry, and all four P donors as well.[35] The result of the decrease in symmetry from O_h to D_{4h} on the ligand-field states is shown in Figure 7.

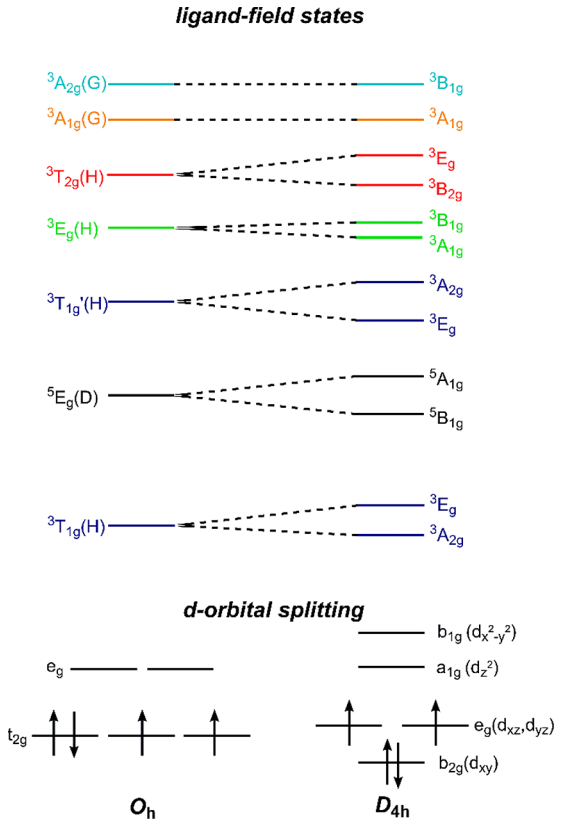

Figure 7. Ligand-field correlation diagram from O_h to D_{4h} symmetry showing low-lying triplet and quintet states. The relative ordering of states is illustrative, and they can be matched with those shown in Figure 6, with use of the same color scheme. The d orbital splitting shown at the bottom is qualitatively that seen in *trans*-[$CrCl_2(dmpe)_2$], so that the ground state is $^3A_{2g}$.

The above estimate for 10*Dq* means that the combination of $\varepsilon_{\sigma,\pi Cl}$ and $\varepsilon_{\sigma,\pi P}$ should roughly equal this value, including π-bonding, which is assumed to be symmetrical (i.e., cylindrical) for both the chlorido and phosphine ligands, donating for the former and accepting for the latter. If we make further the qualitative assumption that π-donation by the chlorido ligands is roughly equal in magnitude to π-acceptance by the phosphine ligands, then the net effect is a lowering in energy of the d_{xy} orbital (b_{2g}) and little effect on the d_{xz} and d_{yz} orbitals (e_g),[36] as shown in Figure 7 (bottom). The challenge is that, even in D_{4h} symmetry, the number of states is large and can become interleaved; namely, that closely spaced $^{1,3}E_g$ and $^{1,3,5}A,B_{(1,2)g}$ states are not separated as in Figure 7 (top), which moreover omits the singlet states for clarity. Moreover, even with the above simplification, there are five variables: one interelectronic repulsion parameter (since C/B is fixed at 4.1) and four bonding parameters ($\varepsilon_{\sigma,\pi Cl}$ and $\varepsilon_{\sigma,\pi P}$), with only three d−d bands being observed. Nevertheless, it is possible to find a solution, by no means unique, that provides a reasonable model for the electronic absorption spectrum. Use of the parameters (values in cm^{-1}) B = 585.4, C = 2400.2, $\varepsilon_{\sigma Cl}$ = 5522.3, $\varepsilon_{\pi Cl}$ = 574.9, $\varepsilon_{\sigma P}$ = 5790.4, and $\varepsilon_{\pi P}$ = −536.0 gives an exact match to the observed bands with the following assignments (in D_{4h} symmetry, with O_h parentage:[37] $^3A_{2g}(^3T_{1g}) \rightarrow {}^1B_{1g}(^1E_g)$ at 6980 cm^{-1}, $^3A_{2g}(^3T_{1g}) \rightarrow {}^1E_g(^1T_{2g})$ at 9060 cm^{-1}, and $^3A_{2g}(^3T_{1g}) \rightarrow {}^3E_g(^3T_{2g})$ at 15980 cm^{-1}. All $g \rightarrow g$ transitions in D_{4h} are technically dipole forbidden, but the use of point group D_4 shows that $A_2 \rightarrow A_1$ is dipole allowed with z polarization and $A_2 \rightarrow E$ is dipole allowed with x, y polarization, while $A_2 \rightarrow A_2$, B_1, and B_2 are all forbidden, so that the two higher energy transitions are dipole allowed by these criteria. The fit value for B is 74% of the free-ion value,[31] thus, a plausible nephelauxetic effect,[38] and the bonding parameters are plausible as well.[39,40] Specifically, the dmpe ligand is a stronger σ-donor and weaker π-acceptor than PPh_3, at least in comparison with $MCl_2(PPh_3)_2$ (M = Co^{II},[41] Ni^{II}[42]), which is as expected for these alkyl versus aryl (and chelating versus monodentate) phosphines.[43] An edited listing of the Ligfield[25] output is given in Table S3A. Finally, it is possible to use idealized D_{2h} symmetry, on the basis of the intrachelate ∠P−Cr−P average values (see Table S2). Prior to fitting in this orthorhombic symmetry, we can use the same fit parameters as derived for D_{4h} symmetry, but now with the XRD-based D_{2h} symmetry. This model gives calculated bands at 6697 and 9270 cm^{-1}—each still close (within 300 cm^{-1}) to the observed NIR bands—and two bands at 15624 and 16151 cm^{-1}, which average to 15888 cm^{-1}—the observed visible band energy. Fitting, however, requires either bracketing the observed bands previously assigned to $^{1,3}E_g$ transitions, arbitrarily selecting only one to fit (either $^{1,3}B_{2g}$ or $^{1,3}B_{3g}$, the ground state being $^3B_{1g}$ in this point group symmetry),[44] or having the fit program contrive to fit both simultaneously, noting that in D_{2h} symmetry there are now 100 states (5 quintet, 45 triplet, and 50 singlet states). The last of these methods is successful, and the results are given in Table S4, but the fit parameters appear less reasonable than those obtained originally. Thus, the use of D_{2h} symmetry adds merely "heat and no light" to the discussion. Further insight is provided using quantum chemical theory (QCT) calculations, as given in the next section.

Finally, SOC can be included to model the observed ZFS. Given that the fit value of B was ∼74% of the free-ion value, we can employ the same reduction in ζ, for which the free-ion value is 229 cm^{-1}.[45] Therefore, use of ζ = 168 cm^{-1} gives a ground state spin singlet and an excited state spin doublet at 7.36 cm^{-1}. This corresponds to D = +7.36 cm^{-1}, which is essentially the same as the experimental value from frozen solution HFEPR (the condition most relevant to the optical spectrum), D = +7.39 cm^{-1}. The results of this calculation using Ligfield showing only the lowest states is given in Table S3B in the Supporting Information. Because of the assumed D_{4h} symmetry, there is no rhombic ZFS, but this effect, as seen by HFEPR, is quite small (E/D = 0.0126), validating the approximation of axial (4-fold) symmetry. Use of the D_{2h} model also gives the observed ZFS, D = +7.36 cm^{-1}, now with E = +0.16 cm^{-1}, although a smaller SOC is required, ζ = 141 cm^{-1} (62% of the free-ion value), and the results are given in Table S4B.

Quantum Chemical Theory (QCT): Geometry Optimizations. To complement the ligand-field theory approach, we performed both DFT and *ab initio* QCT computations to examine the ZFS and excited states of *trans*-[$CrCl_2(dmpe)_2$]. Before delving into those computations, we note that calculated spin Hamiltonian parameters are often very sensitive to the particular molecular structure employed in the calculation. An extreme example is provided by the simple *trans*-[$(py)_4TiCl_2$] coordination complex, where D values calculated using the CASSCF/NEVPT2 method for structural models obtained

https://doi.org/10.1021/acs.inorgchem.1c02471
Inorg. Chem. 2021, 60, 17865−17877

from X-ray crystallography and a DFT calculation using the popular B3LYP functional differed by nearly an order of magnitude (D = −58.4 and −6.23 cm^{-1}, respectively).[10] We therefore performed a geometry optimization of *trans*-[$CrCl_2(dmpe)_2$] in order to assess the influence of modest differences between DFT-optimized and X-ray structures on the calculated spin Hamiltonian parameters. The metric parameters from the DFT optimizations are compared with those from the X-ray structure in Table 1. All calculated bond lengths between the Cr^{II} center and coordinating atoms are within 0.02 Å of the experimental values, and bond angles involving coordinating atoms and the metal center show deviations of less than 2°. Thus, the DFT structures are in excellent agreement with the solid-state structure.

Table 1. Bond Lengths (Å) and Bond Angles (deg) for *trans*-[$CrCl_2(dmpe)_2$] as Determined by X-ray Crystallography (This Work) and DFT Calculations Using Three Different Density Functionals

	exptl	TPSSh-D3	B3LYP-D3	M06-L
Cr−P	2.364	2.351	2.384	2.360
	2.371	2.362	2.377	2.351
Cr−Cl	2.350	2.340	2.370	2.367
Cl−Cr−Cl	180.0	180.0	180.0	180.0
Cl1−Cr−P	P1: 88.18	P1: 86.49	P1: 88.79	P1: 89.34
	P1A: 91.82	P1A: 93.51	P1A: 91.21	P1A: 90.66
	P2:91.23	P2:90.35	P2:92.63	P2:93.11
	P2A: 88.77	P2A: 89.65	P2A: 87.37	P2A: 86.89
P1−Cr−P	P1A: 180.0	P1A: 180.0	P1A: 180.0	P1A: 180.0
	P2: 83.09	P2: 82.97	P2: 83.15	P2: 82.93
	P2A: 96.91	P2A: 97.03	P2A: 96.85	P2A: 97.07

Quantum Chemical Theory: Electronic Structure and Ligand-Field Excited States. The 3d-orbital splitting pattern predicted for *trans*-[$CrCl_2(dmpe)_2$] from spin-unrestricted DFT computations is shown in Figure 8. The compositions of these MOs are summarized in Table 2. The general MO splitting pattern is in accordance with that expected for a complex of approximate D_{4h} symmetry and is in qualitative agreement with the results of LFT (see Table S3). Although the actual symmetry of *trans*-[$CrCl_2(dmpe)_2$] is lower than D_{4h}, we will nonetheless employ symmetry labels from this point group in our discussion of the orbitals and states of this complex, as was done in the LFT section above. The lowest-energy Cr 3d MO is $b_{2g}(d_{xy})$, which is doubly occupied (Figure 8 and Table 2). Both the α- and β-spin $b_{2g}(d_{xy})$ orbitals show significant mixing with the phosphorus orbitals of the two dmpe ligands. The $b_{2g}(d_{xy},d_{yz})$ MOs lie at slightly higher energy than the $b_{2g}(d_{xy})$ MO and are singly occupied. The lack of true D_{4h} symmetry for *trans*-[$CrCl_2(dmpe)_2$] leads to a splitting of the components of the $e_g(d_{xz},d_{yz})$ MOs by ∼0.1−0.3 eV (∼800−2400 cm^{-1}), with the larger splitting being observed for the β-spin MOs. The $e_g(d_{xz},d_{yz})$ orbitals show π-interactions with the axial chloride ligands and contain a modest admixture of P character from the dmpe ligands (Table 2). For the α-spin $e_g(d_{xz},d_{yz})$ MOs, the admixture of ∼18% chloride character reveals enhanced Cr−Cl covalency in comparison to the corresponding Ti−Cl interactions in the recently examined *trans*-[$TiCl_2(tmeda)_2$] complex. In the latter complex, the $e_g(d_{xz},d_{yz})$ MOs showed only 4−8% chloride character.[11] The $a_{1g}(d_{z^2})$ and $b_{1g}(d_{x^2-y^2})$ MOs of *trans*-[$CrCl_2(dmpe)_2$] are both unoccupied and lie 1−3 eV (8000−24000 cm^{-1}) above the $b_{2g}(d_{xy})$ and $e_g(d_{xz},d_{yz})$ MOs (Figure 8 and Table 2). The $a_{1g}(d_{z^2})$ MO is dominated by a σ-antibonding interaction with chloride ligands, with modest (∼6%) contributions from the P atoms. The $b_{1g}(d_{x^2-y^2})$ MO, which is the highest energy Cr 3d orbital, is σ-antibonding with respect to the equatorial dmpe ligands and carries ∼20% P character. The 0.5 eV (4000 cm^{-1}) splitting between $a_{1g}(d_{z^2})$ and $b_{1g}(d_{x^2-y^2})$ reflects the relatively strong Cr−P interactions in the latter MO.

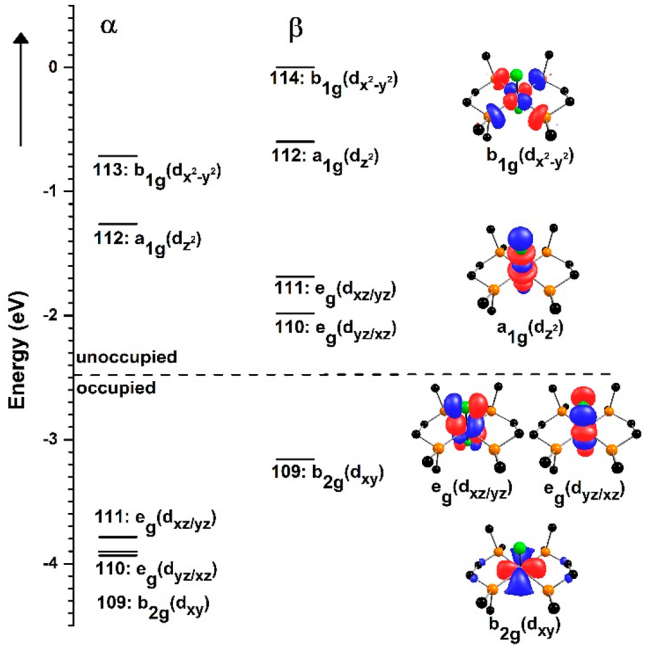

Figure 8. Cr 3d-orbital splitting pattern for *trans*-[$CrCl_2(dmpe)_2$] from spin-unrestricted DFT calculations.

The ligand-field excited states of *trans*-[$CrCl_2(dmpe)_2$] were examined using CASSCF/NEVPT2 computations. This method provides an excellent balance of computational efficiency and accuracy and has been employed to treat both the excited and ground state properties of a variety of transition-metal complexes. Our CASSCF/NEVPT2 calculations for *trans*-[$CrCl_2(dmpe)_2$] employed an active space of the five Cr-based 3d MOs and the fully occupied bonding counterparts of the $a_{1g}(d_{z^2})$ and $b_{1g}(d_{x^2-y^2})$ to give a total of 8 electrons in 7 MOs. The calculations considered 5 quintet, 45 triplet, and 50 singlet states. To aid in our presentation of the CASSCF/NEVPT2 results, we refer back to Figure 7, which illustrates how some of the triplet and quintet O_h parent states split in D_{4h} symmetry. The lowest-energy $^3T_{1g}(H)$ state splits into $^3A_{2g}(^3T_{1g})$ and $^3E_g(^3T_{1g})$ terms, with $^3A_{2g}(^3T_{1g})$ expected as the ground term. At higher energy there are a multitude of additional triplet states (i.e., $^3T_{1g}'$, ^3E_g, $^3T_{2g}$, $^3A_{1g}$, and $^3A_{2g}$ in O_h symmetry), many of which derive from the same ^3H free-ion term as $^3T_{1g}(H)$. The lowest-energy quintet state is $^5E_g(D)$, which splits into $^5B_{1g}$ and $^5A_{1g}$ terms in D_{4h} symmetry. While a number of singlet states interleave these low-lying triplet and quintet states, we will discuss only those single states that contribute to the zero-field splitting of *trans*-[$CrCl_2(dmpe)_2$] (*vide infra*).

The energies of the lowest-lying triplet and quintet states from the CASSCF/NEVPT2 computations are given in Table 3. In

https://doi.org/10.1021/acs.inorgchem.1c02471
Inorg. Chem. 2021, 60, 17865−17877

Table 2. Molecular Orbital Symmetry Labels, Energies (eV), and Percent Compositions Based on Spin-Unrestricted DFT Computations for *trans*-[$CrCl_2(dmpe)_2$]

MO	symmetry label (in D_{4h})	occupancy	energy (eV)	composition (%)		
				Cr 3d[a]	Cl 3p+3s[b]	P 3p+3s+3d[c]
109α	$b_{2g}(d_{xy})$	1.0	−3.9340	75.7	0.8	13.6
110α	$e_g(d_{xz/yz})$	1.0	−3.9039	73.1	18.0	3.8
111α	$e_g(d_{yz/xz})$	1.0	−3.7851	76.2	17.2	2.4
112α	$a_{1g}(d_{z^2})$	0.0	−1.2615	64.0	17.4	6.6
113α	$b_{1g}(d_{x2-y^2})$	0.0	−0.7133	55.0	0.4	23.6
109β	$b_{2g}(d_{xy})$	1.0	−3.1601	66.0	0.0	21.0
110β	$e_g(d_{xz/yz})$	0.0	−1.9841	67.5	10.0	13.0
111β	$e_g(d_{yz/xz})$	0.0	−1.6870	75.1	8.6	9.2
112β	$a_{1g}(d_{z^2})$	0.0	−0.5986	64.2	12.8	5.6
114β	$b_{1g}(d_{x^2-y^2})$	0.0	0.0015	53.9	0.0	19.8

[a]Sum of all Cr 3d contributions to this MO. [b]Sum of all Cl 3p and 3s contributions to this MO. [c]Sum of all P 3s, 3p, and 3d contributions to this MO.

this table we have labeled the states according to the D_{4h} point group, and we include the parent O_h states in parentheses. (In the Supporting Information, we show an alternative to Table 3, Table S9, where the states are arranged first by the parent O_h states from which they derive.) Figure 9 shows a plot of the relative energies of the lowest-lying states. The CASSCF/NEVPT2 computations predict a $^3A_{2g}(^3T_{1g})$ ground state for *trans*-[$CrCl_2(dmpe)_2$] (Table 3). This ground state arises from a $(b_{2g})^2(e_g)^2(a_{1g})^0(b_{1g})^0$ configuration, which is consistent with the DFT computations (Figure 8) and with LFT (see Table S3). The ground state is single reference, containing a 97% contribution from the leading configuration.

The CASSCF/NEVPT2 calculations predict a cluster of triplet, singlet, and quintet states between roughly 10000 and 13000 cm^{-1} (Figure 9 and Table 3). The lowest-lying triplet excited states of *trans*-[$CrCl_2(dmpe)_2$] are predicted at 10878 and 12598 cm^{-1} and are components of the $^3E_g(^3T_{1g})$ state. Thus, these states derive from the same O_h parent state ($^3T_{1g}$) as the $^3A_{2g}$ ground state (Figure 7). Each component of the $^3E_g(^3T_{1g})$ state arises from a $(b_{2g})^1(e_{g1})^3(a_{1g})^0(b_{1g})^0$ configuration and is therefore related to the $^3A_{2g}(^3T_{1g})$ configuration by a $b_{2g} \rightarrow e_g$ one-electron excitation. The lowest-lying quintet states of *trans*-[$CrCl_2(dmpe)_2$] flank the $^3E_g(^3T_{1g})$ states (Table 3). These states are at 10474 and 11759 cm^{-1} and are attributed to the $^5B_{1g}$ and $^5A_{1g}$ states that arise from the ^5E_g parent state of O_h symmetry. The $^1A_{1g}(^1E_g)$ and $^1B_{2g}(^1T_{2g})$ states are also found in this region at 9424 and 10932 cm^{-1}, respectively.

The next cluster of ligand-field excited states for *trans*-[$CrCl_2(dmpe)_2$] is predicted at roughly 16000−19500 cm^{-1} (Table 3 and Figure 9). This cluster contains the singlet excited states $^1A_{1g}(^1A_{1g})$ and $^1E_g(^1T_{2g})$. Triplet excited states for *trans*-[$CrCl_2(dmpe)_2$] are predicted at 15675 and 16800 cm^{-1}. These excited states have a $(b_{2g})^2(e_g)^1(a_{1g})^1(b_{1g})^0$ configuration, which allows us to attribute these states to the ^3E_g components of the $^3T_{1g}'$ O_h parent state (Figure 7). Relative to the ground configuration, these states consist of an $e_g \rightarrow a_{1g}$ one-electron excitation. The $^3T_{1g}'$ O_h parent state also gives rise to a $^3A_{2g}$ state in D_{4h} symmetry (Figure 7). From the CASSCF/NEVPT2 computations, this state is at 27353 cm^{-1}, a significantly higher energy than that for $^3E_g(^3T_{1g}')$. The different configurations of the $^3E_g(^3T_{1g}')$ and $^3A_{2g}(^3T_{1g}')$ states account for this large splitting. While each state corresponds to a $t_{2g} \rightarrow e_g$ excitation in O_h symmetry, in D_{4h} symmetry the ^3E_g state corresponds to an $e_g \rightarrow a_{1g}$ excitation, while the higher-energy $^3A_{2g}$ state corresponds to a $b_{2g} \rightarrow a_{1g}$ excitation. Thus, the lower energy of the b_{2g} MO relative to the e_g MOs account in part for the large energy difference between these states.

At higher energy, between 25000 and 32000 cm^{-1}, the CASSCF/NEVPT2 computations for *trans*-[$CrCl_2(dmpe)_2$] predict nine triplet excited states, three singlet excited states, and two quintet excited states (Table 3 and Figure 9). This high density of triplet excited states is expected on the basis of a d^4 Tanabe−Sugano type of diagram, which predicts a cluster of $^3E(2)$, $^3T_2$, $^3A_1$, and $^3A_2$ states at similar energies, as shown in Figure 6 and Figures S9−S11.

Quantum Chemical Theory: Ground-State Spin Hamiltonian Parameters. Using a minimalist active space of just four electrons in the five Cr 3d-based MOs (CAS(4,5)), the CASSCF/NEVPT2 method predicts $D = +7.81$ cm^{-1} and $E/D = 0.001$ (Table 4). When the NEVPT2 correction is not included, the D value is reduced to +5.77 cm^{-1}. The values including the NEVPT2 correction are very close to the experimental parameters of $D = +7.36(2)$ cm^{-1} and $E/D = 0.0007$ (solid), 0.012 (solution). Thus, the CASSCF/NEVPT2 method is nicely able to reproduce the experimental values using a very small active space, which is consistent with LFT that uses only the d^4 basis set, only indirectly including covalency.

With the use of a slightly larger CAS(8,7) active space, which includes the doubly occupied bonding MOs of the Cr d_{z^2} and $d_{x^2-y^2}$ orbitals, the CASSCF/NEVPT2 method predicts $D = +7.31$ cm^{-1} and $E/D = 0.003$. These values are nearly identical with their experimental counterparts, noting the small difference between solid state and frozen solution data. With this active space, we obtain $\mathbf{g} = [1.992, 1.996, 2.003]$ ($g_{avg} = 1.997$), which are also in good agreement with experiment (Table 4; $g_{avg} = 1.997$ for solid state complex). In conclusion, the combined experimental and theoretical results indicate, as we have noted previously,[46] that g values in non-Kramers-ion systems are notoriously uninformative in that these are generally isotropic and often very close to the free electron value ($g_e = 2.002$—to the precision meaningful here), especially for d^4 systems (usually high spin). Only the ZFS provides useful information on the electronic structure.

The main difference between the calculated D values from the CAS(8,7) and CAS(4,5) calculations are in their contributions to D from the spin−orbit and spin−spin terms (D_{SOC} and D_{SSC}), respectively. For transition-metal complexes, D_{SOC} is typically the dominant term, with contributions from D_{SSC} amounting to

https://doi.org/10.1021/acs.inorgchem.1c02471
Inorg. Chem. 2021, 60, 17865−17877

Table 3. Ligand-Field Excited States of *trans*-[$CrCl_2(dmpe)_2$] from CASSCF/NEVPT2 Computations: Energies and Contributions to Zero-Field Splitting Parameters *D* and *E*[a]

D_{4h} state[b]	energy	D	E
$^3A_{2g}(^3T_{1g})$	0		
$^1A_{1g}(^1E_g)$	9424	0.09	0.00
$^5B_{1g}(^5E_g)$	10474	0.00	0.00
$^3E_g(^3T_{1g})$	10878	1.41	0.39
	12598	0.36	−0.34
$^1B_{2g}(^1T_{2g})$	10932	0.00	0.00
$^5A_{1g}(^5E_g)$	11759	0.00	0.00
$^3E_g(^3T_{1g})$	15675	1.12	−1.10
	16800	1.06	1.05
$^1A_{1g}(^1A_{1g})$	17087	2.90	0.00
$^1E_g(^1T_{2g})$	18045	−0.43	−0.47
	19482	−0.42	0.45
$^1E_g(^1T_{2g})$	23612	−0.66	0.64
	25044	−0.63	−0.62
$^3A_{1g}(^3E_g)$	25613	−0.01	0.00
$^3B_{1g}(^3E_g)$	25922	0.00	0.00
$^3A_{1g}(^3A_{1g})$	27121	0.00	0.00
$^3A_{2g}(^3T_{1g})$	27353	0.00	0.00
$^3B_{2g}(^3T_{2g})$	27857	−0.16	0.00
$^5E_g(^5T_{2g})$	27950	0.00	0.00
	29086	0.00	0.00
$^3E_g(^3T_{2g})$	28766	0.04	0.04
	29820	0.04	−0.04
$^3B_{1g}(^3A_{2g})$	29025	−0.19	0.00
$^1A_{1g}(^1A_{1g})$	29570	0.72	0.00
$^3B_{1g}(^3E_g)$	30744	−0.60	0.00
$^3A_{1g}(^3E_g)$	31242	−0.01	0.00
$^5B_{2g}(^5T_{2g})$	37118	0.00	0.00

[a]All values in cm^{-1}. [b]Parent state in O_h symmetry given in parentheses. See Table S9 for ordering by these parent states.

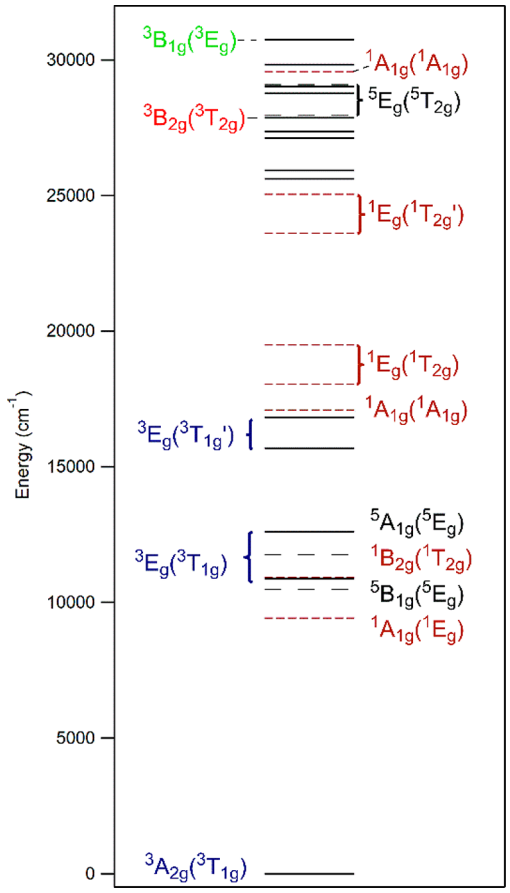

Figure 9. Relative energies of ligand-field excited states of *trans*-[$CrCl_2(dmpe)_2$] from CASSCF/NEVPT2 computations. For clarity, only selected states are labeled. The color scheme corresponds to that in Figures 6 and 7.

~10% of the total D value. Calculations for *trans*-[$CrCl_2(dmpe)_2$] using either active space reveal that the D_{SOC} and D_{SSC} terms have opposing signs (Table 4). However, the smaller CAS(4,5) calculations predict much larger magnitudes for the D_{SOC} and D_{SSC} terms. For the CAS(8,7) active space, the magnitude of the D_{SSC} value is much smaller, roughly 10% of D_{SOC}. Thus, the "correctness" of the total D value using the CAS(4,5) active space likely results from some cancellation of error in the D_{SOC} and D_{SSC} contributions (i.e., the magnitudes of both are overestimated but this inaccuracy is canceled by the opposing signs of these terms). Note that the simple LFT model does not include SSC yet fortuitously gave an exact match to the experimental D value.

We also performed CAS(8,7) calculations for DFT-optimized structures of *trans*-[$CrCl_2(dmpe)_2$], and the spin Hamiltonian parameters for these calculations are in Table 4. From the CASSCF/NEVPT2 calculations, the D values for the geometry-optimized structures range from +6.93 to +7.48 cm^{-1}, in very good agreement with the experimental value (+7.36(2) cm^{-1}). In fact, the greatest deviation, observed for the structure optimized using the TPSSh-D3 functional, is still within 6% of the experimental value and therefore quite respectable. The E/D values for the optimized structures are all very axial and are also in good agreement with experiment. Thus, for *trans*-[$CrCl_2(dmpe)_2$], the modest differences between the crystal structure and DFT-derived coordinates merely have a very small effect on the calculated ZFS parameters.

Focusing on the calculations using the crystal structure coordinates of *trans*-[$CrCl_2(dmpe)_2$] and the CAS(8,7) active space, we examined contributions to the ground state ZFS parameters for individual excited states (Table 3; see also Table S9 for an alternative organization). The two low-energy ^3E_g states near 11000 and 16000 cm^{-1} each provide positive contributions to D of +1.77 and +2.18 cm^{-1}, respectively. The contributions to the E values from the components of the ^3E_g

https://doi.org/10.1021/acs.inorgchem.1c02471
Inorg. Chem. 2021, 60, 17865−17877

Table 4. Experimental and Calculated Zero-Field Splitting Parameters (D in cm^{-1}) and g Values

geometry	method	D_{tot}[a]	D_{SOC}[a]	D_{SSC}[a]	E/D	g
	HFEPR (solid)[b]	+7.36(2)			~0	1.998(5), 1.998(5), 1.989(7)
	HFEPR (solution)	+7.36(2)			0.012	1.999(5), 2.00(1), 2.00(1)
X-ray	CAS(4,5)	+5.77	+9.57	−3.80	0.001	1.983, 1.989, 2.000
X-ray	CAS(4,5)/NEVPT2	+7.81	+11.62	−3.81	0.001	1.978, 1.984, 2.001
X-ray	CAS(8,7)	+5.34	+6.18	−0.84	0.004	1.980, 1.984, 2.003
X-ray	CAS(8,7)/NEVPT2	+7.31	+8.14	−0.83	0.003	1.992, 1.996, 2.003
TPSSh-D3	CAS(8,7)	+4.97	+5.86	−0.89	0.011	1.981, 1.986, 2.002
	CAS(8,7)/NEVPT2	+6.93	+7.81	−0.88	0.008	1.981, 1.986, 2.002
B3LYP-D3	CAS(8,7)	+5.52	+6.56	−1.04	0.003	1.978, 1.984, 2.003
	CAS(8,7)/NEVPT2	+7.48	+8.52	−1.04	0.002	1.978, 1.984, 2.003
M06-L	CAS(8,7)	+5.08	+5.88	−0.80	0.012	1.980, 1.985, 2.003
	CAS(8,7)/NEVPT2	+7.02	+7.83	−0.81	0.009	1.980, 1.985, 2.003
X-ray	DFT-BP	+4.64	+3.18	+1.46	0.007	2.001, 2.006, 2.008
X-ray	DFT-B3LYP	+2.11	+0.42	+1.68	0.037	1.999, 2.000, 2.004
		+3.57[c]	+1.88[c]	+1.69[c]	0.021[c]	1.999, 2.000, 2.003[c]
X-ray	DFT-TPSS	+4.12	+2.61	+1.51	0.004	2.000, 2.005, 2.007
X-ray	DFT-TPSSh	+5.67	+4.05	+1.61	0.007	2.000, 2.002, 2.005
		+5.62[c]	+4.01[c]	+1.61[c]	0.005[c]	2.000, 2.002, 2.004[c]
X-ray	DFT-M06	+7.28	+5.61	+1.67	0.051	1.996, 1.998, 2.011
		+7.19[c]	+5.52[c]	+1.67[c]	0.047[c]	1.994, 1.997, 2.007[c]
X-ray	DFT-M06-L	+3.85	+2.21	+1.64	0.013	2.000, 2.002, 2.004
ideal D_{4h}	LFT[d]	+7.36	+7.36	—	0	—
ideal D_{2h}	LFT[d]	+7.35	+7.35	—	0.021	—

[a]D values in cm^{-1}. [b]The positive sign of D was determined from magnetometry and by comparison with frozen solution HFEPR measurements; $|E|$ = 0.005 cm^{-1}, and so E/D < 0.001 cm^{-1}. An axial **g** tensor was assumed. [c]Calculations utilized def2-TZVPP basis sets for all atoms. [d]See LFT section and Tables S3 and S4 for parameters used. The LFT calculations do not include SSC.

states are of similar magnitudes but opposite signs and thus cancel each other out. An additional, positively signed contribution to D comes from the $^1A_{1g}(^1A_{1g})$ state at 17087 cm^{-1}, which contributes +2.90 cm^{-1} (Table 3). More modest, negatively signed contributions to D come from a pair of ^1E_g states at roughly 19000 and 24000 cm^{-1} (−0.85 and −1.29 cm^{-1}, respectively). These contributions tend to decrease D, but only slightly. The components of these E_g states also provide contributions to E that effectively cancel. Additional contributions to D come from the higher-energy $^3B_{1g}(^3A_{2g})$, $^1A_{1g}(^1A_{1g})$, and $^3B_{1g}(^3E_g)$ states. On the basis of this analysis, we conclude that the positive sign of D arises largely from contributions from ^3E_g and $^1A_{1g}$ states, while negatively signed contributions from ^1E_g states tend to decrease the magnitude of D. The near-perfect cancellation of contributions arising from differently signed contributions to E from the components of E_g states gives rise to the very small E/D value.

For comparison, we also calculated spin Hamiltonian parameters for *trans*-[$CrCl_2(dmpe)_2$] using coupled-perturbed (CP) DFT calculations. Although CP-DFT calculations are typically less reliable than the CASSCF/NEVPT2 method for such parameters, it is informative to determine if the CP-DFT approach is effective for a "simple" coordination complex with relatively high symmetry and modest ZFS. The results of CP-DFT calculations, employing a variety of different density functionals, are collected in Table 4. We draw two main conclusions from the ZFS parameters from the CP-DFT computations. First, while the magnitudes of D vary depending on the identity of the density functional, all functionals properly reproduce the experimental sign of D, and all functionals predict a nearly axial system. The meta-hybrid-GGA functionals (TPSSh and M06) provide the D values closest to those in the experiment (+5.67 and +7.28 cm^{-1}, respectively), with the M06 method being the most accurate functional in our series. The pure functionals (the meta-GGA TPSS and GGA BP functionals) perform slightly worse, with D between +4 and +5 cm^{-1}, and the M06-L and B3LYP functionals most significantly underestimate the magnitude of D (D = +3.85 and +2.11 cm^{-1}).

The second main conclusion that we draw from the CP-DFT results are that the D_{SOC} and D_{SSC} contributions differ markedly from those predicted by the CASSCF/NEVPT2 method. Regardless of the functional chosen, the CP-DFT calculations predict a D_{SSC} value of roughly +1.6 cm^{-1}. Thus, the variation in the D values from the CP-DFT calculations comes almost completely from the D_{SOC} term. In comparison, the CASSCF/NEVPT2 calculations predict a negatively signed contribution from D_{SSC} (Table 4), with much larger D_{SOC} contributions. If one assumes the CASSC/NEVPT method to be more reliable in predicting the signs and magnitudes of the D_{SOC} and D_{SSC} terms, then the excellent D value predicted by the M06 functional is an example of DFT computations getting the correct answer for the wrong reason. Specifically, the DFT methods predict the wrong sign for D_{SSC} but compensate by predicting a small D_{SOC} term.

Finally, we performed CP-DFT calculations for the B3LYP, TPSSh, and M06 functionals using the larger def2-TZVPP basis sets on all atoms. While the D and E/D values for the TPSSh and M06 functionals showed a very modest dependence on basis set size (changing by less than 2%), the D value for the B3LYP functional increased notably from +2.11 to +3.57 cm^{-1}. This increase is due to a nearly 5-fold increase in the magnitude of the D_{SOC} term.

■ CONCLUSIONS

Chelating diphosphines are among the most ubiquitous ligands in inorganic/organometallic chemistry, with dmpe being the paramount of these. The synthesis by Wilkinson and co-workers

https://doi.org/10.1021/acs.inorgchem.1c02471
Inorg. Chem. 2021, 60, 17865−17877

of the series of *trans*-[$MX_2(dmpe)_2$] (M = most $3d^{+2}$ ions, X = halide) complexes was a landmark in the area.[1,3] Subsequent work by Girolami and co-workers[4−7] and others[23,47] built on this foundation. Advances in both experimentation, in particular HFEPR to access integer spin (non-Kramers) ions, and in theory, in particular *ab initio* methods, have now made it worthwhile to revisit some of these complexes with the goal of a definitive determination of their electronic structure. Complexes with P donors, as opposed to those with N donors, have been relatively less explored by these combined experimental and theoretical methods. Here, *trans*-[$CrX_2(dmpe)_2$] has been subjected to low-temperature XRD (the original structure being at room temperature[1]), variable-temperature magnetometry, and HFEPR spectroscopy in both the solid state and frozen solution. In addition to classical LFT, state of the art QCT, in particular *ab initio* methods, have been used to analyze the experimental results. The complex *trans*-[$CrX_2(dmpe)_2$] is more computationally challenging than it might seem given its relatively simple structure with approximate D_{4h} symmetry. Unlike a typical distorted-octahedral Cr^{II} complex, the complex has an $S = 1$ spin ground state, rather than $S = 2$. Theory quantitatively shows how this $^3A_{2g}$ ground state is the result of the ligand field exerted by the phosphine and chlorido ligands. The observed electronic transitions are well reproduced by theory, but more importantly, so are the spin Hamiltonian parameters of the triplet ground state, which are measured precisely by HFEPR, with the ZFS given by $D = +7.36\ cm^{-1}$ with a remarkably small rhombic component ($E/D \approx 0.01$), despite the distortion imposed by the dmpe chelates. The g values are isotropic, close to 2.00, and are thus essentially uninformative. The origin of the ZFS is described in detail using CASSCF/NEVPT2 computations, which reveal contributions from particular excited states to the ground state ZFS. From these computations, the magnitude of D in this system is controlled by a set of low-lying ^3E_g states and a $^1A_{1g}$ state. A careful comparison among theoretical methods demonstrates in this Cr^{II} system the optimal approach to an electronic structure determination. This study thus provides a roadmap toward understanding paramagnetic early-transition-metal phosphine complexes in general and contributes to the awareness of the importance of spin ground state variation in all types of coordination complexes.[13]

■ ASSOCIATED CONTENT

Supporting Information

The Supporting Information is available free of charge at https://pubs.acs.org/doi/10.1021/acs.inorgchem.1c02471.

Additional crystallographic and other structural comparative data, details of experimental and computational methods, HFEPR spectra and diagrams, and results from LFT and QCT calculations (PDF)

Accession Codes

CCDC 2101839 contains the supplementary crystallographic data for this paper. These data can be obtained free of charge via www.ccdc.cam.ac.uk/data_request/cif, or by emailing data_request@ccdc.cam.ac.uk, or by contacting The Cambridge Crystallographic Data Centre, 12 Union Road, Cambridge CB2 1EZ, UK; fax: +44 1223 336033.

■ AUTHOR INFORMATION

Corresponding Authors

Timothy A. Jackson − *Department of Chemistry, University of Kansas, Lawrence, Kansas 66045, United States;* orcid.org/0000-0002-3529-2715; Email: taj@ku.edu

Joshua Telser − *Department of Biological, Physical and Health Sciences, Roosevelt University, Chicago, Illinois 60605, United States;* orcid.org/0000-0003-3307-2556; Email: jtelser@roosevelt.edu

Authors

Eva M. Zolnhofer − *Department of Chemistry and Pharmacy, Inorganic Chemistry, Friedrich-Alexander University Erlangen-Nürnberg (FAU), 91058 Erlangen, Germany*

Adedamola A. Opalade − *Department of Chemistry, University of Kansas, Lawrence, Kansas 66045, United States*

Frank W. Heinemann − *Department of Chemistry and Pharmacy, Inorganic Chemistry, Friedrich-Alexander University Erlangen-Nürnberg (FAU), 91058 Erlangen, Germany;* orcid.org/0000-0002-9007-8404

Karsten Meyer − *Department of Chemistry and Pharmacy, Inorganic Chemistry, Friedrich-Alexander University Erlangen-Nürnberg (FAU), 91058 Erlangen, Germany;* orcid.org/0000-0002-7844-2998

J. Krzystek − *National High Magnetic Field Laboratory, Florida State University, Tallahassee, Florida 32310, United States;* orcid.org/0000-0001-6088-1936

Andrew Ozarowski − *National High Magnetic Field Laboratory, Florida State University, Tallahassee, Florida 32310, United States;* orcid.org/0000-0001-6225-9796

Complete contact information is available at: https://pubs.acs.org/10.1021/acs.inorgchem.1c02471

Notes

The authors declare no competing financial interest.

■ ACKNOWLEDGMENTS

T.A.J. acknowledges funding from the US NSF (CHE-1900384). K.M. acknowledges generous support from the Friedrich-Alexander University Erlangen-Nürnberg (FAU). A portion of this work was performed at the National High Magnetic Field Laboratory, which is supported by NSF Cooperative Agreement DMR-1644779 and the State of Florida.

■ REFERENCES

(1) Girolami, G. S.; Wilkinson, G.; Galas, A. M. R.; Thornton-Pett, M.; Hursthouse, M. B. Synthesis and properties of the divalent 1,2-bis(dimethylphosphino)ethane (dmpe) complexes $MCl_2(dmpe)_2$ and $MMe_2(dmpe)_2$ (M = Ti, V, Cr, Mn, or Fe). X-Ray crystal structures of $MCl_2(dmpe)_2$ (M = Ti, V, or Cr), $MnBr_2(dmpe)_2$, $TiMe_{1.3}Cl_{0.7}(dmpe)_2$, and $CrMe_2(dmpe)_2$. *J. Chem. Soc., Dalton Trans.* **1985**, 1339−1348.

(2) Not every permutation was prepared: for X = Cl, M = Ti, V, Cr; for X = Br and I, M = Mn; for X = Me, M = Ti (as $Me_{1.3}Cl_{0.7}$), V, Cr, Mn. The complex where M = Cr, X = Me had also been reported in an earlier communication.

(3) Girolami, G. S.; Salt, J. E.; Wilkinson, G.; Thornton-Pett, M.; Hursthouse, M. B. Alkyl, hydride, and dinitrogen 1,2-bis-(dimethylphosphino)ethane complexes of chromium. Crystal structures of $Me_2Cr(dmpe)_2$, $CrH_4(dmpe)_2$, and $Cr(N_2)_2(dmpe)_2$. *J. Am. Chem. Soc.* **1983**, *105*, 5954−5956.

(4) Jensen, J. A.; Wilson, S. R.; Schultz, A. J.; Girolami, G. S. Divalent titanium chemistry. Synthesis, reactivity, and x-ray and neutron

diffraction studies of $Ti(BH_4)_2(dmpe)_2$ and $Ti(CH_3)_2(dmpe)_2$. *J. Am. Chem. Soc.* **1987**, *109*, 8094−8096.

(5) Morris, R. J.; Girolami, G. S. On the 5-donor ability of early transition metals: evidence that trialkylphosphines can engage in l-back-bonding and x-ray structure of the titanium(II) phenoxide $Ti(OPh)_2(dmpe)_2$. *Inorg. Chem.* **1990**, *29*, 4167−4169.

(6) Jensen, J. A.; Girolami, G. S. Synthesis, characterization, and x-ray crystal structures of the divalent titanium complex $Ti(r^2\text{-}BH_4)_2(dmpe)_2$ and the unidentate tetrahydroborate complex $V(h^1\text{-}BH_4)_2(dmpe)_2$. *Inorg. Chem.* **1989**, *28*, 2107−2113.

(7) Morris, R. J.; Wilson, S. R.; Girolami, G. S. Vanadium(II) alkyls. Synthesis and X-ray crystal structures of *trans*-$VMe_2(dmpe)_2$ and *cis*-$V(CH_2SiMe_3)_2(dmpe)_2$. *J. Organomet. Chem.* **1994**, *480*, 1−9.

(8) Edema, J. J. H.; Duchateau, R.; Gambarotta, S.; Hynes, R.; Gabe, E. Novel titanium(II) amine complexes L_4TiCl_2 [L = 1/2 *N,N,N',N'*-tetramethylethylenediamine (TMEDA), 1/2 *N,N,N'*-trimethylethylenediamine, pyridine, 1/2 2,2′-bipyridine]: synthesis and crystal structure of monomeric *trans*-$(TMEDA)_2TiCl_2$. *Inorg. Chem.* **1991**, *30*, 154−156.

(9) Araya, M. A.; Cotton, F. A.; Matonic, J. H.; Murillo, C. A. An Efficient Reduction Process Leading to Titanium(II) and Niobium(II): Preparation and Structural Characterization of *trans*-$MCl_2(py)_4$ Compounds, M = Ti, Nb, and Mn. *Inorg. Chem.* **1995**, *34*, 5424−5428.

(10) Wijeratne, G. B.; Zolnhofer, E. M.; Fortier, S.; Grant, L. N.; Carroll, P. J.; Chen, C.-H.; Meyer, K.; Krzystek, J.; Ozarowski, A.; Jackson, T. A.; Mindiola, D. J.; Telser, J. Electronic Structure and Reactivity of a Well-Defined Mononuclear Complex of Ti(II). *Inorg. Chem.* **2015**, *54*, 10380−10397.

(11) Zolnhofer, E. M.; Wijeratne, G. B.; Jackson, T. A.; Fortier, S.; Heinemann, F. W.; Meyer, K.; Krzystek, J.; Ozarowski, A.; Mindiola, D. J.; Telser, J. Electronic Structure and Magnetic Properties of a Titanium(II) Coordination Complex. *Inorg. Chem.* **2020**, *59*, 6187−6201.

(12) As an aside on the vagaries of nomenclature, tmeda and dmpe are both $Me_2ECH_2CH_2EMe_2$, (E = N, P, respectively) yet have common names that originate in one case in classical coordination chemistry and in the other in organometallic chemistry and thus seem to be more different than they actually are.

(13) Halcrow, M. A. Manipulating metal spin states for biomimetic, catalytic and molecular materials chemistry. *Dalton Trans.* **2020**, *49*, 15560−15567.

(14) Using the IUPAC definition,[15,16] a d^4 complex in O_h symmetry is high spin when $S = 2$ ($t_{2g}^3e_g^1$) and low-spin when $S = 1$ ($t_{2g}^4e_g^0$).

(15) Chalk, S. J. *IUPAC Compendium of Chemical Terminology*, 2nd ed. (the "Gold Book"); https://goldbook.iupac.org/terms/view/LT06788 (accessed September 20, 2021).

(16) de Bolster, M. W. G. Glossary of terms used in bioinorganic chemistry (IUPAC Recommendations 1997). *Pure Appl. Chem.* **1997**, *69*, 1251−1304.

(17) Telser, J.; Pardi, L. A.; Krzystek, J.; Brunel, L.-C. EPR spectra from 'EPR-silent' species: high-field EPR spectroscopy of aqueous chromium(II). *Inorg. Chem.* **1998**, *37*, 5769−5775.

(18) Dobe, C.; Andres, H.-P.; Tregenna-Piggott, P. L. W.; Mossin, S.; Weihe, H.; Janssen, S. Variable temperature inelastic neutron scattering study of chromium(II) Tutton salt: manifestation of the $^5E\otimes e$ Jahn-Teller effect. *Chem. Phys. Lett.* **2002**, *362*, 387−396.

(19) Dobe, C.; Noble, C.; Carver, G.; Tregenna-Piggott, P. L. W.; McIntyre, G. J.; Barra, A.-L.; Neels, A.; Janssen, S.; Juranyi, F. Electronic and molecular structure of high-spin d^4 complexes: experimental and theoretical study of the $[Cr(D_2O)_6]^{2+}$ cation in Tutton's salts. *J. Am. Chem. Soc.* **2004**, *126*, 16639−16652.

(20) Forshaw, A. P.; Smith, J. M.; Ozarowski, A.; Krzystek, J.; Smirnov, D.; Zvyagin, S. A.; Harris, T. D.; Karunadasa, H. I.; Zadrozny, J. M.; Schnegg, A.; Holldack, K.; Jackson, T. A.; Alamiri, A.; Barnes, D. M.; Telser, J. Low-Spin Hexacoordinate Mn(III): Synthesis and Spectroscopic Investigation of Homoleptic Tris(pyrazolyl)borate and Tris(carbene)borate Complexes. *Inorg. Chem.* **2013**, *52*, 144−159.

(21) Boča, R. Zero-field splitting in metal complexes. *Coord. Chem. Rev.* **2004**, *248*, 757−815.

(22) Krzystek, J.; Ozarowski, A.; Telser, J. Multi-frequency, high-field EPR as a powerful tool to accurately determine zero-field splitting in high-spin transition metal coordination complexes. *Coord. Chem. Rev.* **2006**, *250*, 2308−2324.

(23) Karunadasa, H. I.; Arquero, K. D.; Berben, L. A.; Long, J. R. Enhancing the Magnetic Anisotropy of Cyano-Ligated Chromium(II) and Chromium(III) Complexes via Heavy Halide Ligand Effects. *Inorg. Chem.* **2010**, *49*, 4738−4740.

(24) Bain, G. A.; Berry, J. F. Diamagnetic Corrections and Pascal's Constants. *J. Chem. Educ.* **2008**, *85*, 532−536.

(25) Bendix, J. Ligfield. In *Comprehensive Coordination Chemistry II*; Lever, A. B. P., Ed.; Elsevier: 2003; Vol. 2, Fundamentals: Physical Methods, Theoretical Analysis, and Case Studies, pp 673−676.

(26) Neese, F. *ORCA - an ab initio, Density Functional and Semiempirical Program Package, Ver. 4.0*; Max Planck Institute for Chemical Energy Conversion: 2017.

(27) Neese, F. The ORCA program system. *Wiley Interdiscip. Rev.: Comput. Mol. Sci.* **2012**, *2*, 73−78.

(28) Ricci, G.; Forni, A.; Boglia, A.; Sonzogni, M. New Chromium(II) Bidentate Phosphine Complexes: Synthesis, Characterization, and Behavior in the Polymerization of 1,3-Butadiene. *Organometallics* **2004**, *23*, 3727−3732.

(29) Hoppeé, J. I. Effective magnetic moment. *J. Chem. Educ.* **1972**, *49*, 505.

(30) TIP can also be included in the fits using only magnetic data. If g_{iso} is fixed at 1.98 (the room-temperature fluid solution value), then a successful fit results with $D = +6.775$ cm^{-1} and TIP = 138.7×10^{-6} cm^3 mol^{-1}; if g_{iso} is fixed at 1.995 (the HFEPR average value), then a successful fit results with $D = +7.046$ cm^{-1} and TIP = 63.5×10^{-6} cm^3 mol^{-1}, the values of which are essentially the same as those from HFEPR.

(31) Brorson, M.; Schäffer, C. E. Orthonormal interelectronic repulsion operators in the parametrical d^q model. Application of the model to gaseous ions. *Inorg. Chem.* **1988**, *27*, 2522−2530.

(32) The free-ion parentage of this state is complicated; it originates in ^3H but becomes very mixed so that at $Dq = 2000$ cm^{-1} it is <40% from ^3H, ∼30% from $^3F_{a,b}$, and the balance from ^3G and $^3P_{a,b}$.

(33) The free-ion parentage that accounts for >80% at $Dq = 1500$ cm^{-1} is given; $^3A_{1g}$ is a pure ^3G state, and $^3A_{2g}$ is pure ^3F.

(34) Alternate assignments were considered: assignment to $^3T_{1g} \rightarrow 3T_{1g}'$(see Figure 7) gives $B = 430$ cm^{-1} and $\varepsilon_\sigma = 5690$ cm^{-1}, and assignment to $^3T_{1g} \rightarrow {}^3A_{2g}$ gives $B = 570$ cm^{-1} and $\varepsilon_\sigma = 5010$ cm^{-1}.

(35) Molecule 2 is chosen for the AOM because, using the criterion of Cr−P bond lengths, it better approximates ideal D_{4h} symmetry than molecule 1 does. The actual Cl−Cr−P angles are ∼88 and ∼92° and the intrachelate P3−Cr−P4 angle is 82.64°; see Table S2.

(36) Miessler, G. L.; Fischer, P. J.; Tarr, D. A. *Inorganic Chemistry*, 5th ed.; Pearson: 2014; p 682.

(37) The O_h parentage of the many states in D_{4h} symmetry can be determined only for those at the lower relative energy range ($\lesssim$22000 cm^{-1}), such as those given here, and at the highest energy range ($\gtrsim$65000 cm^{-1}), where the states are of no relevance. Only if the tetragonal splitting were small could such a determination be confidently made across all states, which number 43 in O_h (2 quintet, 18 triplet, and 23 singlet states) but number 76 in D_{4h} (4 quintet, 33 triplet, and 39 singlet states).

(38) Jørgensen, C. K. The Nephelauxetic Series. *Prog. Inorg. Chem.* **2007**, *4*, 73−124.

(39) Bridgeman, A. J.; Gerloch, M. The Interpretation of Ligand Field Parameters. *Prog. Inorg. Chem.* **2007**, *45*, 179−281.

(40) Gerloch, M.; Slade, R. C. In *Ligand-Field Parameters*; Cambridge University Press: 1973.

(41) Bone, A. N.; Widener, C. N.; Moseley, D. H.; Liu, Z.; Lu, Z.; Cheng, Y.; Daemen, L. L.; Ozerov, M.; Telser, J.; Thirunavukkuarasu, K.; Smirnov, D.; Greer, S. M.; Hill, S.; Krzystek, J.; Holldack, K.; Aliabadi, A.; Schnegg, A.; Dunbar, K. R.; Xue, Z.-L. Applying Unconventional Spectroscopies to the Single-Molecule Magnets, $Co(PPh_3)_2X_2$ (X = Cl, Br, I): Unveiling Magnetic Transitions and Spin-Phonon Coupling. *Chem. - Eur. J.* **2021**, *27*, 11110−11125.

(42) Krzystek, J.; Park, J.-H.; Meisel, M. W.; Hitchman, M. A.; Stratemeier, H.; Brunel, L.-C.; Telser, J. EPR Spectra from "EPR-Silent" Species: High-Frequency and High-Field EPR Spectroscopy of Pseudotetrahedral Complexes of Nickel(II). *Inorg. Chem.* **2002**, *41*, 4478−4487.

(43) Tolman, C. A. Steric effects of phosphorus ligands in organometallic chemistry and homogeneous catalysis. *Chem. Rev.* **1977**, *77*, 313−348.

(44) All g → g transitions in D_{2h} are technically dipole forbidden, but the use of point group D_2 shows that $B_1 \rightarrow B_2$ is dipole allowed with x polarization and $B_1 \rightarrow B_3$ is dipole allowed with y polarization, while $B_1 \rightarrow A$ is now dipole allowed with z polarization and only $B_1 \rightarrow B_1$ is dipole forbidden.

(45) Bendix, J.; Brorson, M.; Schäffer, C. E. Accurate empirical spin orbit coupling parameters ζ_{nd} for gaseous nd^q transition metal ions. The parametrical multiplet term model. *Inorg. Chem.* **1993**, *32*, 2838−2849.

(46) Telser, J.; Krzystek, J.; Ozarowski, A. High-frequency and high-field electron paramagnetic resonance (HFEPR): a new spectroscopic tool for bioinorganic chemistry. *JBIC, J. Biol. Inorg. Chem.* **2014**, *19*, 297−318.

(47) Halepoto, D. M.; Holt, D. G. L.; Larkworthy, L. F.; Leigh, G. J.; Povey, D. C.; Smith, G. W. Spin crossover in chromium(II) complexes and the crystal and molecular structure of the high spin form of bis[1,2-bis(diethylphosphino)ethane]di-iodochromium(II). *J. Chem. Soc., Chem. Commun.* **1989**, 1322−1323.

■ NOTE ADDED AFTER ASAP PUBLICATION

This paper was originally published ASAP on November 1, 2021, with an error in the TOC graphic. The corrected version was reposted on November 5, 2021.

https://doi.org/10.1021/acs.inorgchem.1c02471
Inorg. Chem. 2021, 60, 17865−17877